ANGULAR TRAPPING OF A MIRROR USING RADIATION PRESSURE

By

David B. Kelley

B.S. Massachusetts Institute of Technology, Cambridge, MA, 2010

Disertation

Submitted in Partial Fulfillment of the Requirements

for the degree of

Doctor of Philosophy in Physics

Syracuse University

September 2015

ANGULAR TRAPPING OF A MIRROR USING RADIATION PRESSURE

By

David B. Kelley

B.S. Massachusetts Institute of Technology, Cambridge, MA, 2010

Disertation

Submitted in Partial Fulfillment of the Requirements

for the degree of

Doctor of Philosophy in Physics

Syracuse University

September 2015

Approved : _____

Prof. Stefan Ballmer

Date : _____

ABSTRACT

Alignment control in gravitational-wave detectors has consistently proven to be a difficult problem due to the stringent noise contamination requirement for the gravitational wave readout and the radiation-pressure induced angular instability in Fabry-Perot cavities (Sidles-Sigg instability). I present the development, implementation, and measurement of a dual-carrier control scheme which uses radiation pressure to control a suspended mirror, trapping it in the longitudinal degree of freedom and one angular degree of freedom.

Contents

List of Tables

List of Figures

Preface

The work presented in this thesis stems from my participation in the LIGO Scientific Collaboration (LSC). This work does not reflect the scientific opinion of the LSC and it was not reviewed by the collaboration.

The theory of optical trapping in two degrees of freedom in chapter 1 is based on

A. Perreca *et al.*, "Multi-dimensional optical trapping of a mirror," *Phys. Rev. D* **89** (2014) 122002.

Chapter 2 is based on material from

David B. Kelley *et al.*, "Observation of photo-thermal feed-back in a stable dual-carrier optical spring," to be submitted to *Phys. Rev. D*.

Chapter 3 is based on

David B. Kelley *et al.*, "Angular Trap Demonstraion," to be submitted to *Phys. Rev. D*

Acknowledgments

Thanks for the music.....

to

my parents and Emma

Chapter 1

Introduction

The Laser Interferometer Grvitational-Wave Observatory is a cool thing...

Chapter 2

Things photothermal

2.1 Introduction

The Advanced Laser Interferometer Gravitational-Wave Observatory (aLIGO) [3], together with its international partners Virgo [4] and KAGRA [5], aim to directly observe gravitational waves emitted by astrophysical sources such as coalescencing of black hole and neutron star binary systems. The installation of the Advanced LIGO detectors is completed, and commissioning towards the the first observation run is ongoing. Preliminary astrophysical data is expected in 2015. The sensitivity of those advanced gravitational-wave detectors in the observation band is limited by the quantum noise of light and the thermal noise associated with mirror coatings. A contributor to the thermal noise, expected to dominate in future cryogenic gravitational-wave detectors, is thermo-optic noise [6, 7, 1]. It is caused by dissipation through thermal diffusion.

The same physics also leads to an intensity noise coupling, known in the literature as photo-thermal effect [8]. The low frequency behaviour of the photo-thermal effect was predicted in [7] and experimentally measured in a Fabry-Perot cavity in by De Rosa et. al. [9]. The physics relevant for the the high frequency behaviour, dominated by the details of the coating, was investigated in [1] in the context of studying thermo-optic noise. It was extended to a full model of the photo-thermal transfer function in [10]. Here we explore the thermo-optic effect in the context of an optical spring. The coupling acts as an additional feed-back path. The phase of the coupling becomes important and can directly affect the stability of the optical spring resonance. We can

exploit this dependence for a precision measurement of the photo-thermal coupling, even if it is driven by the residual few-ppm absorption of a high-quality optic.

The desire to lower the quantum noise in the gravitational-wave observation band has driven the power circulating in the Advanced LIGO arm cavities up to about 800 kW. The high laser power, in turn, couples the angular suspension modes of the two cavity mirrors. This Sidles-Sigg instability [11] creates a soft (unstable) and a hard mode, whose frequency increases with the intra-cavity power. The detector's angular control system must control the soft and damp the hard mode, and at the same time must not contaminate the observation band, starting at 10 Hz in the case of Advanced LIGO. Future gravitational wave detectors aim to extend the observational band to even lower frequencies, further aggravating this limitation. We previously proposed a model [12] to overcome the angular instabilities, based on a dual-carrier optical spring scheme demonstrated by Corbitt et al., in 2007 at the LIGO laboratory [13]. The proposed angular trap setup uses two dual-carrier beams to illuminate two suspended optical cavities which share a single end mirror. As first step towards the experimental demonstration of the scheme we built and operated a prototype, single-cavity optical trap, capable of controlling the cavity length only [14]. The data presented in this paper was taken with this prototype. The next version of the angular trap setup will also allow us to measure the photo-thermal effect on a folding mirror. Heinert et. al. [15] predicted excess thermal noise for folding mirrors due to transverse heat diffusion. The result has not yet been experimentally confirmed, but since the same physics will also lead to an enhanced photo-thermal transfer function, the prediction can be verified with a photo-thermal transfer function measurement.

The paper is structured as follows: Sections 2.2 and 2.3 will review the idea of a dual-carrier optical spring and the photo-thermal effect respectively. Section 2.4 describes the experimental setup and we discuss the result in section 2.5. Finally, section 2.6 suggests a coating modification to make a single-carrier optical spring feasable.

2.2 Dual-carrier optical spring

A Fabry-Perot cavity detuned from resonance couples the intra-cavity power linearly to the mirror position. The response is delayed by the cavity storage time. The

resulting optical spring constant is given by [12].

$$K_{OS}^{\text{1field}} \approx K_0 \frac{1}{1+\frac{\delta^2}{\gamma^2}-\frac{\Omega^2}{\gamma^2}+i2\frac{\Omega}{\gamma}} \tag{2.1}$$

$$K_0 = P_0 t_1^2 r_2^2 \frac{8kr_1r_2}{c(1-r_1r_2)^3} \frac{\frac{\delta}{\gamma}}{(1+\frac{\delta^2}{\gamma^2})} \tag{2.2}$$

where P_0 is the incident power, corrected for mode-matching losses, $k = 2\pi/\lambda$ is the wave vector of the light, t_i and r_i are the mirror amplitude transmissivity and reflectivity for input coupler ($i = 1$) and end mirror ($i = 2$), and γ, δ and Ω are the cavity line, cavity detuning, and mechanical frequency. The value of K_{OS} lies in either the 2nd or 4th quadrant of the complex plane, and the associated radiation pressure force creates either a anti-restoring and damping (red detuning) or a restoring and anti-damping force (blue detuning) [16].

Two spatially overlapping optical fields, the carrier and sub-carrier, with opposite detuning sign and with an opportune power ratio can be used to cancel the instability [13]. The total optical spring K_{OS} is the sum of the individual springs

$$K_{OS} = K_{OS}^{c} + K_{OS}^{sc} \tag{2.3}$$

Where K_{OS}^{c} and K_{OS}^{sc} are given by equation 2.1. The dual-carrier optical spring can be tuned to lie in the 1st quadrant for the frequency band of interest. When acting on a suspended cavity end mirror with mass m and mechanical suspension spring constant K_m the optical spring becomes a feed-back loop with a closed loop response function

$$\frac{x}{F_{ext}} = \frac{1}{-m\Omega^2 + K_m + K_{OS}} \tag{2.4}$$

The tunability of the optical spring K_{OS} in both magnitude and phase allows experimental fine-tuning of the poles of equation 2.4 to lie exactly on the real axis, resulting in an infinite Q of the optical spring (critical stablility). Experimentally this can be done up to a maximum Q, above which the measured transfer function data no longer permits distinguishing between a stable and an unstable spring. The phase of the total spring constant at resonance can then be determined with a precision given by $1/Q$. The suspension mechanical spring constant has to have a positive imaginary part, but it can be designed to be very small. Loss angles of 10^{-5} are easily

achievable, and are further diluted by the magnitude of the ratio of K_{OS}/K_m. The contribution to the phase of the total spring constant from the mechanical suspension is thus expected to be negligible. The imaginary part of the optical spring K_{OS} on the other hand is closely related to its real part through equations 2.3 and 2.1, and is very accurately predicted based on the resonance frequency, carrier to sub-carrier power ratio as well as the detuning of carrier and subcarrier, i.e. only power ratios and frequencies. As a result, any deviation in phase from the expectation of equation 2.1 around the optical spring resonance is easily and repeatably observable with a precision given by the inverse of the experimentally resolvable Q, and an accuracy determined only by frequency and power ratio measurements.

2.3 Photo-thermal effect

Power absorption on the surface of an optic leads to an increase of the surface temperature. The depth of the heated layer is given by the diffusion length $d_{\text{diff}} = \sqrt{\kappa/(\rho C \Omega)}$, where κ, C and ρ are the thermal conductivity, heat capacity and density of the material, and Ω is the observation angular frequency. In the large-spot size limit, i.e. $\mathrm{w} \gg d_{\text{diff}}$, and neglecting coating effects, the displacement of the surface is given by (e.g. [7, 10])

$$\triangle z = \bar{\alpha} \int_0^\infty T dz = \bar{\alpha} \frac{j}{i\Omega\rho C} \tag{2.5}$$

where $\bar{\alpha} = 2(1+\sigma)\alpha$ is the effective expansion coefficient under the mechanical constraint that the heated spot is part of a much larger optic [1, 2]. α and σ are the regular linear expansion coefficient and Poisson ratio. $j = P/(\pi \mathrm{w}^2)$ is the absorbed average surface intensity of the Gaussian beam with beam radius w ($1/e^2$ intensity). This simple picture needs two important refinements. First, for frequencies Ω around and below $\Omega_c = 2\kappa/(\rho C \mathrm{w}^2)$ the transverse heat diffusion leads to a multiplicative correction factor to equation 2.5 derived by Cerdonio et al. [7]:

$$I(\Omega/\Omega_c) = \frac{1}{\pi} \int_0^\infty du \int_{-\infty}^\infty dv \frac{u^2 e^{-u^2/2}}{(u^2+v^2)\left(1 + \frac{(u^2+v^2)}{i\Omega/\Omega_c}\right)} \tag{2.6}$$

As expected, for $\Omega \gg \Omega_c$, the correction factor approches 1. For a fused Silica substrate, SiO_2, and a Gaussian beam spot radius of $\mathrm{w} = 161$ μm this correction

becomes large below $\Omega_c/(2\pi) = 10$ Hz, but is measurably different from unity even at 1 kHz. (See fig 1)

Second, for high frequencies, the diffusion length becomes comparable to the coating thickness. Since the optical field is reflected by a dielectric stack, the effective mirror displacement is given by [1, 10]

$$\triangle z = \sum_i \left[\frac{\partial \phi_c}{\partial \phi_i} (\beta_i + \bar{\alpha}_i n_i) + \bar{\alpha}_i \right] \bar{T}_i d_i \tag{2.7}$$

where $\bar{\alpha}_i$, $\beta_i = dn/dT$ and n_i are the constrained effective expansion coefficient, the temperature dependence of the index of refraction, and the index of refraction itself for layer i. $\frac{\partial \phi_c}{\partial \phi_i}$, the dependence of the coating reflected phase on the round trip optical phase in layer i, is always negative, resulting in a sign change and enhancement of the bracket in equation 2.7 for the first few layers. $\bar{T}_i d_i$ is the temperature profile driven by the absorped intensity j, integrated across layer i. For a $Ta_2O_5 : SiO_2$ coating used in gravitational wave detectors we find a measureable enhancement of the photo-thermal transfer function around 1 kHz [10]. Additionally, depending on the detailed absorption profile, a sign change can occur above about 100 kHz.

For the experiment parameters discussed in this paper, i.e. a Gaussian beam spot radius of w = 161 μm and a mirror coating with about 13 doublet layers both effects are relevant in the 100 Hz to 1 kHz band. Their contributions are plotted in figure 1.

2.4 Experimental setup

2.4.1 Cavity

The optical spring cavity is composed of two suspended mirrors in a vacuum chamber, each with radius of curvature RoC = 5 cm and power transmissivity $T = 4.18 \times 10^{-4}$. The measured finesse is 7500±250 and the cavity length is $L_0 = 7.0 \pm 0.2$ cm. We chose a short cavity to minimize frequency noise coupling. The cavity has a free spectral range (FSR) of about 2.14 GHz and cavity pole $f_{pole} = \gamma/(2\pi) = 143$ kHz. The input mirror mass is 300 g, designed to be heavy to make it insensitive to radiation pressure; it is suspended as a single stage pendulum with mechanical resonances, i.e. position, pitch and yaw, close to 1 Hz. The end mirror has a mass of 0.41 ± 0.01 g and is 7.75 mm in diameter. It is suspended with three glass fibers from a 300 g steel ring,

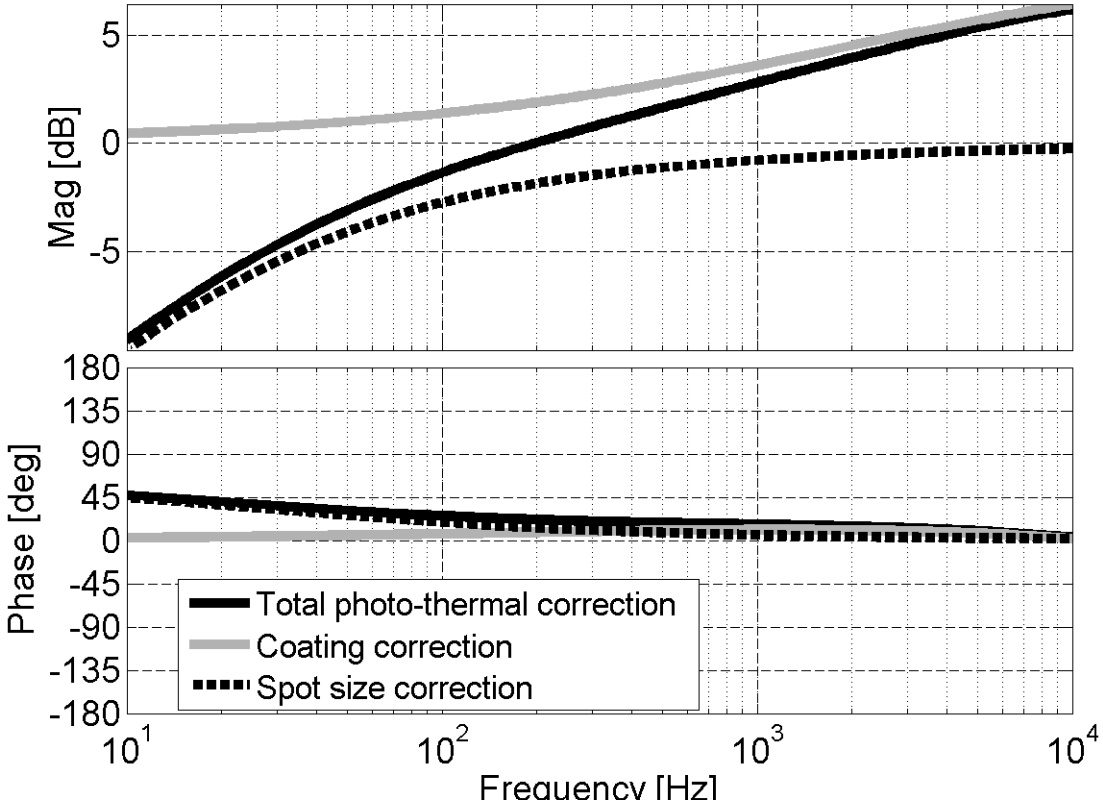

Figure 1 : Correction factors for the photo-thermal transfer function of a fused silica mirror with a dielectric coating (solid black). The solid grey trace is the coating correction for a 13-doublet $\lambda/4$ Ta_2O_5: SiO_2 coating. The dashed black trace shows the effect of a Gaussian beam spot with w = 161 μm radius. To get the full transfer function, multiply with equation 2.5, adding an overall $1/f$ shape. The calculation is based on material parameters show in table 2.

shown in figure 2. The steel ring has diameter of 7.6 cm and is itself suspended. The input mirror is actively controlled by an electronic feedback system, while the end mirror is free to move in the glass suspension abobe its resonance frequency of 18 Hz, and is only subject to the optical spring radiation pressure.

2.4.2 Input field preparation

The optical field incident on the optical spring cavity consists of two beams, a carrier and a subcarrier, as described in Section 2.2. As shown in figure 3, a 1064 nm laser is split into a carrier and a subcarrier beam at the polarizing beam splitter PBS1. In the subcarrier path two acoustic optic modulators (AOMs) are used to impose a

λ_0	1064 nm
Mirror RoC	5.0 cm
L_0	7.0 cm
Spot size	161 μm
FSR	2.14 GHz
Finesse	7500
Cavity Pole	143 KHz

δf_C	213-290 KHz
δf_{SC}	27-36 KHz
P_C input	225-239 mW
P_{SC} input	65-78 mW

Table 1 : Parameters of the optical spring cavity. The range of values for the carrier and subcarrier detuning frequency (δf_C, δf_{SC}) and input power (P_C, P_{SC}) indicate the variation between individual measurements.

relative frequency shift Δ, on the subcarrier beam, leaving it at a set detuning from the carrier beam. Δ is set using an external signal generator (see Sec. 2.4.3). The two beams recombine at PBS2 and proceed towards the Fabry-Perot cavity with opposite polarization. The total power and the power ratio between the carrier and subcarrier beams are set by two half wave-plates $\lambda/2$.

The subcarrier beam is modulated by a 35 MHz electro-optic modulator (EOM). We measure the modulated light reflected by the cavity with a resonant radio-frequency photodiode (RFPD) and then demodulate to read out the cavity length with the Pound-Drever-Hall technique (PDH) [17]. We use the subcarrier to derive a PDH singal because the subcarrier requires less detuning than the carrier. We can use the PDH signal to actuate on the laser and the suspensions to lock the cavity, then turn down the gain and use the PDH signal for readout.

A small offset added to the PDH error signal shifts the locking point of the cavity to the side of the resonance, setting the subcarrier detuning δ_{sc}. We choose to introduce an offset that corresponds to a negative frequency ("red") detuning. Consequently the carrier is positively ("blue") detuned at $\delta_c = \Delta + \delta_{sc}$. An electronic locking servo can be used to process the error signal and feed back to coils, actuating on magnets mounted on the large cavity mirror, and to the laser frequency.

2.4.3 Subcarrier Servo

The high FSR of our cavity (2.14 GHz) meant that available AOMs, with much lower operating frequency ranges (65 to 95 MHz), were not suitable to lock the carrier and

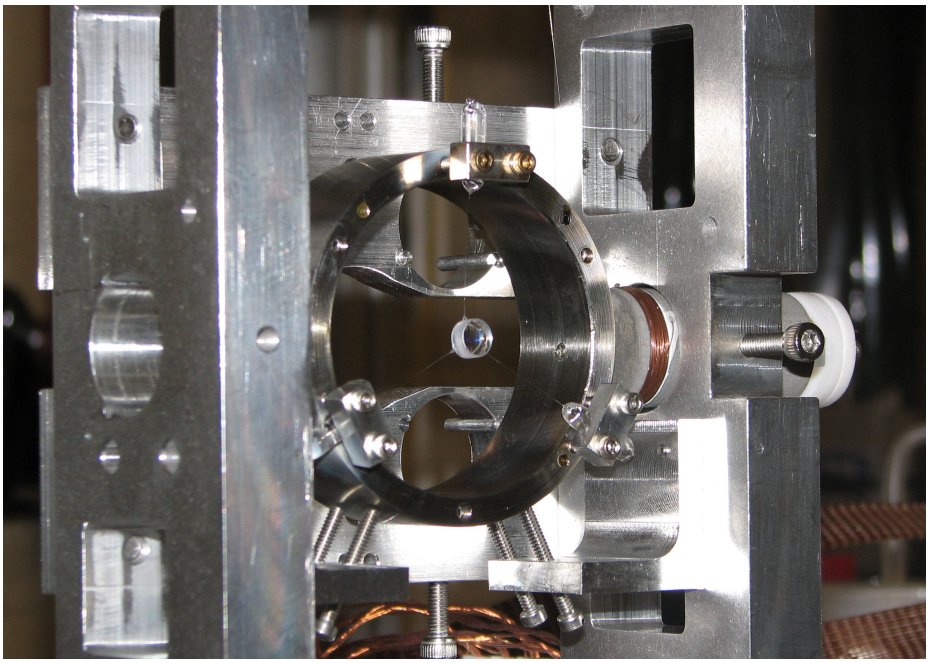

Figure 2 : A picture of the small end mirror suspended from a steel ring by glass fibers. The ring is suspended from a small optics suspension (SOS) with tungsten wire. The SOS provides DC alignment control while allowing the mirror to move freely above the 18Hz resonance of the fiber suspension. The end of the fiber is a small glass nub attached to the mirror with epoxy. This produces a fairly high suspension Q of about $5 \cdot 10^5$. The resulting contribution of damping in the opto-mechanical spring is insignificant compared to the damping from the optical field.

subcarrier on adjacent resonances. However, this same operating range prevents a single AOM from locking the two beams on the same resonance, due to the small cavity linewidth. Thus, we set the subcarrier on the same resonance fringe as the carrier using two AOMs, each one shifting the laser frequency by about 80MHz in opposite directions. One is driven by an 80 MHz crystal oscillator, while the other is driven by a servo-locked Voltage controlled oscillator (VCO) running slightly offset from 80 MHz (see figure 3). To control the offset frequency the 80 MHz signal from the crystal oscillator is mixed with the VCO output, producing a signal at the frequency difference. This difference signal is then mixed with the drive from a function generator, creating the error signal for the servo. The servo drives the frequency modulation input of the VCO, closing the loop and locking the subcarrier beam to a fixed frequency offset from the carrier beam.

This setup significantly suppresses the frequency noise from the VCO. The remaining subcarrier frequency noise (relative to the carrier) is dominated by fluctuations

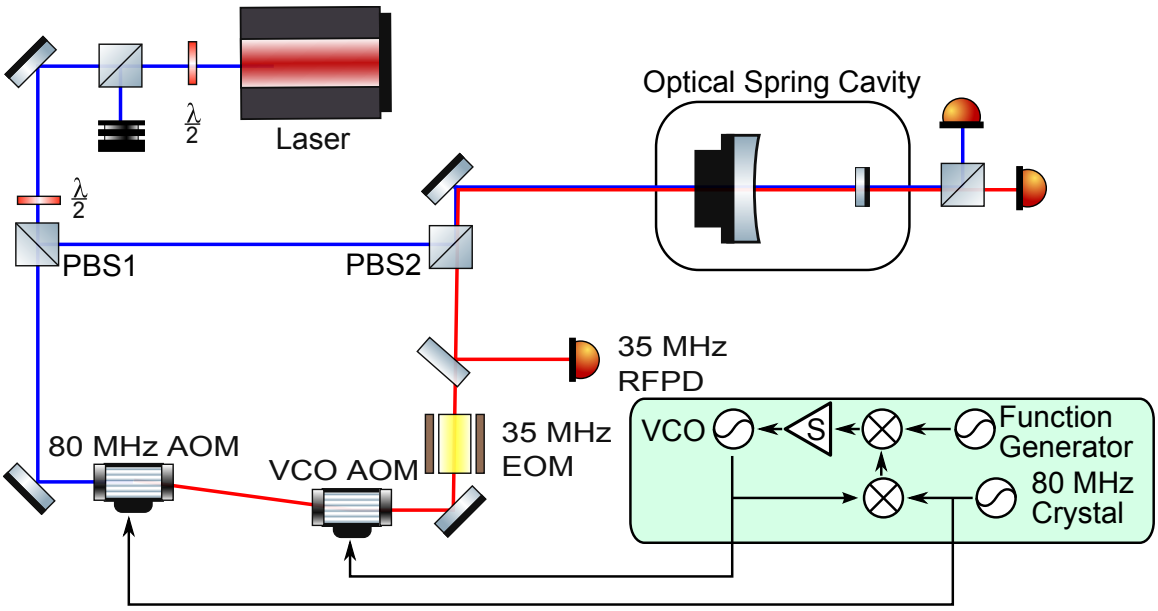

Figure 3 : A schematic layout of the optical trap experiment. The light from the laser is split into the carrier and subcarrier paths at PBS1, with a ratio determined by the $\lambda/2$ plate. The subcarrier path is frequency shifted by two AOMs under the control of the subcarrier servo (described in detail in Section 2.4.3), then recombined with the carrier at PBS2. The co-aligned mode-matched beams enter the cavity, then are individually monitored at the output. We can use the 35 MHz EOM and RFPD in a PDH scheme to read out the cavity length or lock the cavity.

in the path length difference between carrier and sub-carrier, see figure 3.

2.5 Results

Using the setup described in the previous section, we locked the cavity using a PDH error signal from the sub-carrier, feeding back to the laser frequency actuator and, at low frequencies, the heavy input coupler position. In this configuration we fine-tuned the optical spring parameters (carrier and sub-carrier offset and power) and measured the PDH control loop open loop transfer function. Dividing out the known PDH loop sensing and actuation function gives us the closed loop transfer functions of the optical springs (figure 4). While we demonstrated stable and unstable dual-carrier optical springs, these measurements revealed a significantly smaller phase margin of the optical spring than expected based on equation 2.4, suggesting the presence of a non-radiation-pressure feed-back path.

At a few ppm, the absorption A of the mirrors has a very small effect on the cavity

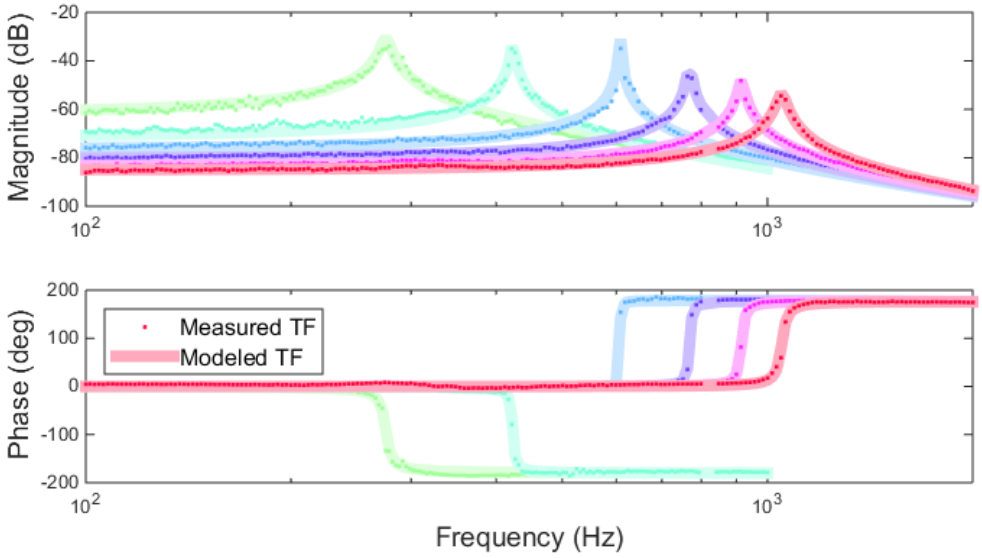

Figure 4 : Data and modeled transfer function for a series of stable and unstable springs. The modeled transfer functions include the full coating and spot size correction, computed with the measured average absorption. Stable springs show a phase drop of 180 degrees at resonance, while unstable springs show a rise of 180 degrees.

finesse and no significant impact on the total transmitted power. However, this small amount of absorption still causes local heating of the optic, driving fluctuations in the surface position of the optic, and thus the cavity length, via the photo-thermal effect. If this is the dominant effect, we should be able to include the photo-thermal effect in our model and fit the model to the data, using the absorption as the free parameter. Given a set of optical spring measurements done under similar conditions, we would then expect to find a consistent absorption coefficient across measurements.

2.5.1 Analysis

For each measured optical spring transfer function we record the carrier and subcarrier transmitted powers, P_{tc} and P_{ts}, the optical spring resonance frequency f_{res}, and the difference between the carrier and subcarrier detunings $df_c - df_s$, which is set by the function generator frequency.

We can then fit the data d using a model m, which includes the photo-thermal effect. In particular we fit the ratio d/m using a least-squares fit to minimize E, the

error.

$$E = \Sigma \left| \frac{d}{m} - 1 \right|^2 \tag{2.8}$$

We fit for a small magnitude offset, the subcarrier detuning df_s, and the absorption A. We assess the fitting errors by modeling the noise in each frequency bin of the transfer function measurement, and propagating this noise through the fit. Four of the optical spring transfer functions had a measurement noise of a little less than 1 dB, while the optical springs at 276 Hz and 422 Hz had a significantly higher noise of about 3 dB. We think this noise is dominated by intra-cavity power fluctuations, most likely due to angular fluctuations.

The remaining parameters (cavity transmitted powers and carrier-sub-carrier frequency spacing) we treat as systematic errors. We propagated their measurment errors through the fit. We used a 2% measurement error for the power measurements and a 1 kHz error for the frequency separation.

After determining the absorption A for each optical spring transfer function measurement, we can take a statistical-error-weighted average to arrive at the most probable absorption coefficient for the mirror. For the full photo-thermal model we measure a consistent absorption of 2.60 ± 0.08 ppm (± 0.06 ppm statistical, ± 0.05 ppm systematic) (see figure 5). The naive $1/f$ model yields an absorption of 3.27 ± 0.10 ppm (± 0.08 ppm statistical, ± 0.06 ppm systematic). The detailed model with coating and spot size corrections is slightly preferred by the data over the naive $1/f$ model, i.e. the result is more consistent with the same absorption at all frequencies. However the errors in our mesurement are too large to make this statement with any sigificant certainty.

Since this measurement is based on the missing optical spring phase on resonance, we can also express the result as extra phase. Near the resonance the optical spring constant is close to real, while the photo-thermal effect is almost purely imaginary. Thus we approximately find for the extra phase ϕ

$$\phi = 2m\Omega^2 \frac{c}{2} \frac{\bar{\alpha}}{\Omega \rho C \mathrm{w}^2 \pi} A I_{\mathrm{corr}} \approx 0.4^\circ \frac{A I_{\mathrm{corr}}}{1 \text{ ppm}} \frac{f}{1 \text{ kHz}} \tag{2.9}$$

Here the leading factor of two accounts for the two mirrors, I_{corr} is the real part of the total correction factor plotted in figure 1, and we used the material parameters for fused silica (see table 2). Figure 6 shows the measured extra phase on resonance,

together with the prediction from the photo-thermal feed-back with the best-fit absorption. The figure also shows the expected phase due to the dual-carrier optical spring, as well as the total phase of the complete model. Finally it is worth mentioning that this is a remarkably precise way to measure the phase of the open loop transfer function - the error bars in figure 6 are as small as 0.04°.

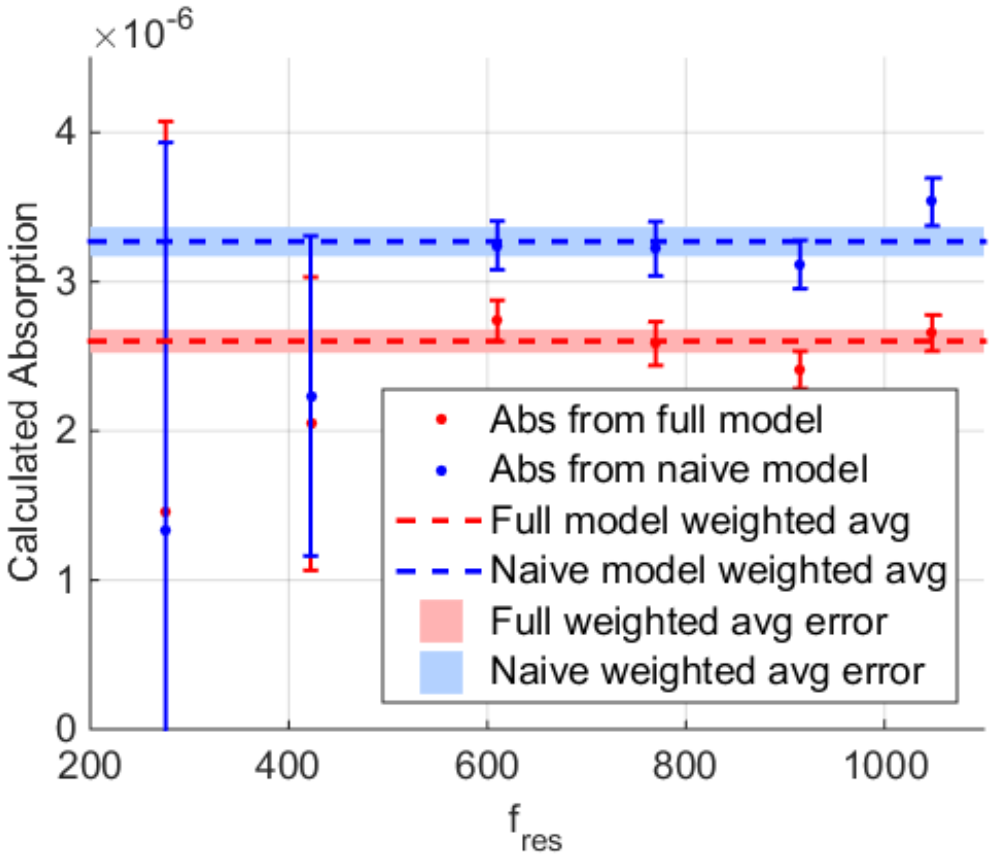

Figure 5 : Absorption fit for naive and full models. The full model absorption is consistent with a constant absorption of 2.60 ± 0.08 ppm. The naive $1/f$ model predicts 3.27 ± 0.10 ppm. The transfer function data for the lowest two resonant frequencies was significantly noisier. Also, at lower frequencies the photo-thermal effect has a smaller effect on the total optical spring. Both effects result in the larger error bars at low frequencies.

2.6 Stable single-carrier optical spring

In the experiment at hand the photo-thermal feed-back always pushed the optical spring resonance closer to instability. Perhaps the most interesting question is whether

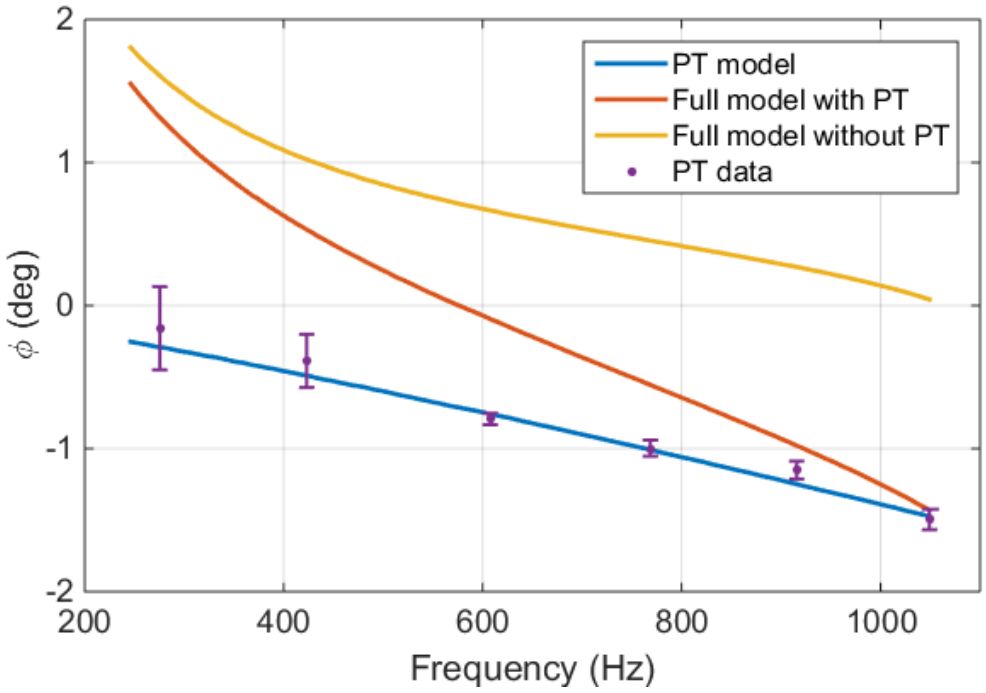

Figure 6 : Feedback phase in the system due to the optical spring and photo-thermal effect. The measured extra phase is consistent with 2.60 ppm of absorption. The error bars are as small as $\pm 0.04°$, a remarkable precision for an open loop transfer function phase measurement.

we can change the sign of this feed-back path and exploit it to stabilize an otherwise unstable optical spring. It was pointed out in [10] that this naturally occurs above about 100 kHz for a regular dielectric coating. At those frequencies the thermal diffusion length only affects the first few layers of the coating, which affect the overall coating reflected phase differently than the rest of the coating. However it is actually quite simple to get this sign inversion to occur at a much lower frequency. Increasing the thickness of the inital half-wavelength SiO_2 layer - but keeping it an odd multiple of half the wavelength - will boost the effect from the first layer, thus lowering the frequency at which this sign inversion occurs. Indeed this effect can be strong enough that the damping effect from the sub-carrier is not needed to generate a stable optical spring. To illustrate this, figure 7 shows a set of six optical springs with parameters identical to the ones shown in figure 4, except that we set the sub-carrier power to zero (i.e. they are single-carrier optical springs), and we increased the first SiO_2 coating layer from 0.5 wavelength to 20.5 wavelength.

Such a modified coating would thus allow detuned self-locking of an optical cavity, using just one laser frequency. It does rely on a small amount (order 1 ppm) of optical absorption in the coating, but this level of absorption is often unavoidable anyway, and does not prevent high-finesse cavities.

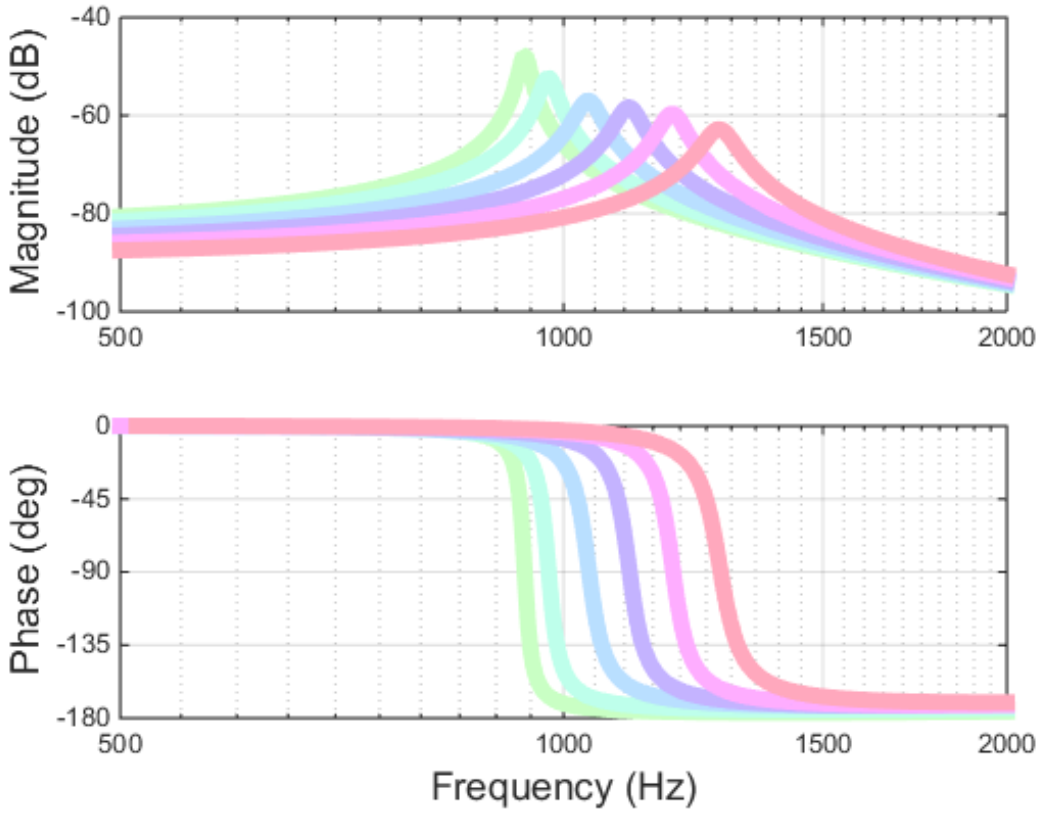

Figure 7 : Stable single-carrier optical springs (no sub-carrier) with modified coating - the first coating layer is 20.5 wavelength thick. See text for details. The six traces otherwise have the same parameters as the best-fit optical springs in figure 4.

2.7 Conclusions

We observed photo-thermal feedback in an experimental optical spring setup for a 0.4 gram mirror. We made measurements for a range of optical spring resonant frequencies, and used a least squares fit to calculate the absorption. The data is consistent with the predictions of the complete model presented in Section 2.3, but only sligthly prefers it over a simple model that ignores any heat diffusion in the

coating and transverse to the optical axis. We also show that a small modification of the first layer of the high-reflectivity coating would be enough to reverse the sign of the photo-thermal feed-back, to the extent that a single-carrier, dynamically and statically stable optical spring becomes feasable.

Repeating the presented measurement with a folding mirror in a cavity should also allow us to confirm the predicted enhancement of thermal noise for folding mirrors [15] . This noise will affect any gravitational-wave interferometer design making use of folding mirrors in the arm cavities [18].

Parameters Ta_2O_5 : SiO_2	Symbol	SiO_2	Ta_2O_5	Unit
Refractive Index (@1064 nm)	n	1.45	2.06	-
Specific Heat	C	746	306	J/kg/K
Density	ρ	2200	6850	kg/m^3
Thermal Conductivity	κ	1.38	33	W/m/K
Thermal expansion coef.	α	0.51	3.6	ppm/K
Thermo-Optic coef. (1μm)	$\beta = \frac{dn}{dT}$	8	14	ppm/K
Poisson ratio	σ	0.17	0.23	-
Youngs Modulus	E	72.80	140	GPa

Table 2 : Parameters for fused silica (SiO_2) and tantulum-pentoxide (Ta_2O_5). The values are taken from [1] and [2].

Chapter 3

Angular

To determine the behavior of a folded optical spring, we can compare it to the standard optical spring derivation [12].

We begin with a folded cavity with three mirrors, shown in fig. 8. The incoming field is E. The average round-trip path length is $L = 4L_0$. We consider microscopic harmonic changes in cavity length d_n corresponding to mirror positions at specific times $d(t)$ moving mirrors M3 and M4 for n odd and even, respectively. The light travel time in one 'arm' is $\tau = \frac{L_0}{c}$.

We can write the round trip path length including the noise as

$$\begin{aligned} L_1 &= 2(2L_0 + d_1 + d_2) \\ L_2 &= 2(4L_0 + d_1 + d_2 + d_3 + d_4) \\ L_3 &= 2(3L_0 + d_1 + d_2 + d_3 + d_4 + d_5 + d_6) \\ &... \end{aligned} \tag{3.1}$$

$$\begin{aligned} d(t) &= x_0 e^{i\Omega t} \\ d_n &= d(t - [(2n-1)\tau + \alpha_n]) \quad \text{and} \end{aligned} \tag{3.2}$$

$$\alpha_n = 2\sum_{l=1}^{n-1} \frac{d_l}{c} - \frac{d_n}{c} \tag{3.3}$$

We define a phase propagation $Y = e^{-i\Omega 2\tau}$ and cavity round trip propagation $X = (r_1 r_2)^2 e^{\frac{-i2\pi L}{\lambda}}$. Neglecting the α_n terms, which are quadratic in d,

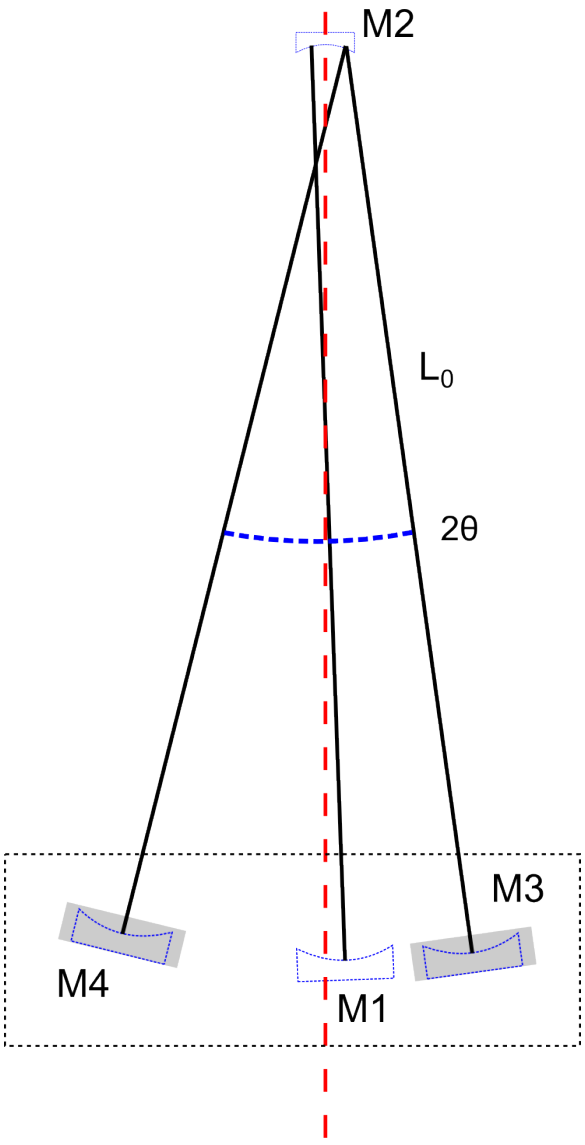

Figure 8 : Layout of the angular trap cavity. Light enters through mirrors M1 and M3.

$$\begin{aligned} d_n &= Y^{2(n-1)} d_1 \\ d_{n+1} &= Y^2 d_n \end{aligned} \tag{3.4}$$

following Antonio,

$$E_{tot} = \frac{t_1 E}{1-X}\left[1 - \frac{4i\pi d_1}{\lambda}\frac{X(1+Y^2)}{1-Y^2X}\right]$$

$$E_{tot} = \frac{t_1 E}{1-X}\left[1 - \frac{4i\pi}{\lambda}\left(\frac{d_1(1+Y^2)}{1-Y^2X} + \frac{\overline{d_1}(1+\overline{Y}^2)}{1-\overline{Y}^2X}\right)\right] \tag{3.5}$$

$d_1 = xY$ so we get the power

$$P = -P_0 t^2\left[\frac{ikY}{(1-\overline{X})(1-X)}\left(\frac{X(1+Y^2)}{1-Y^2X} - \frac{\overline{X}(1+\overline{Y}^2)}{1-Y^2\overline{X}}\right)x + cc\right]? \tag{3.6}$$

Chapter 4

Conclusion

I hope to have found something by this point in the thesis.

Bibliography

[1] M. Evans, S. Ballmer, M. Fejer, P. Fritschel, G. Harry, and G. Ogin. Thermo-optic noise in coated mirrors for high-precision optical measurements. *Phys. Rev. D*, 78:102003, Nov 2008.

[2] M. M. Fejer, S. Rowan, G. Cagnoli, D. R. M. Crooks, A. Gretarsson, G. M. Harry, J. Hough, S. D. Penn, P. H. Sneddon, and S. P. Vyatchanin. Thermoelastic dissipation in inhomogeneous media: loss measurements and displacement noise in coated test masses for interferometric gravitational wave detectors. *Phys. Rev. D*, 70:082003, Oct 2004.

[3] Gregory M Harry and the LIGO Scientific Collaboration. Advanced ligo: the next generation of gravitational wave detectors. *Classical and Quantum Gravity*, 27(8):084006, 2010.

[4] J. Degallaix, T. Accadia, F. Acernese, M. Agathos, A. Allocca, P. Astone, G. Ballardin, F. Barone, M. Bejger, M. G. Beker, M. Bitossi, M. A. Bizouard, M. Blom, F. Bondu, L. Bonelli, R. Bonnand, V. Boschi, L. Bosi, B. Bouhou, C. Bradaschia, M. Branchesi, T. Briant, A. Brillet, V. Brisson, T. Bulik, H. J. Bulten, D. Buskulic, C. Buy, G. Cagnoli, E. Calloni, B. Canuel, F. Carbognani, F. Cavalier, R. Cavalieri, G. Cella, E. Cesarini, E. Chassande-Mottin, A. Chincarini, A. Chiummo, F. Cleva, E. Coccia, P.-F. Cohadon, C. N. Colacino, A. Colla, M. Colombini, A. Conte, J.-P. Coulon, E. Cuoco, S. D'Antonio, V. Dattilo, M. Davier, R. Day, R. De Rosa, G. Debreczeni, W. Del Pozzo, L. Di Fiore, A. Di Lieto, A. Di Virgilio, A. Dietz, M. Drago, G. Endroczi, V. Fafone, I. Ferrante, F. Ferrini, F. Fidecaro, I. Fiori, R. Flaminio, L. A. Forte, J.-D. Fournier, J. Franc, S. Franco, S. Frasca, F. Frasconi, M. Galimberti, L. Gammaitoni, F. Garufi, M. E. Gáspár, G. Gemme, E. Genin, A. Gennai, A. Giazotto, R. Gouaty, M. Granata,

G. M. Guidi, A. Heidmann, H. Heitmann, P. Hello, G. Hemming, P. Jaranowski, R. J. G. Jonker, M. Kasprzack, I. Kowalska, A. Królak, N. Leroy, N. Letendre, T. G. F. Li, M. Lorenzini, V. Loriette, G. Losurdo, E. Majorana, I. Maksimovic, V. Malvezzi, N. Man, M. Mantovani, F. Marchesoni, F. Marion, J. Marque, F. Martelli, A. Masserot, J. Meidam, C. Michel, L. Milano, Y. Minenkov, M. Mohan, N. Morgado, S. Mosca, B. Mours, L. Naticchioni, I. Neri, F. Nocera, L. Palladino, C. Palomba, F. Paoletti, R. Paoletti, M. Parisi, A. Pasqualetti, R. Passaquieti, D. Passuello, M. Pichot, F. Piergiovanni, L. Pinard, R. Poggiani, G. A. Prodi, M. Punturo, P. Puppo, D. S. Rabeling, I. Rácz, P. Rapagnani, V. Re, T. Regimbau, F. Ricci, F. Robinet, A. Rocchi, L. Rolland, R. Romano, Rosiń, D. ska, P. Ruggi, E. Saracco, B. Sassolas, D. Sentenac, L. Sperandio, R. Sturani, B. Swinkels, M. Tacca, L. Taffarello, A. P. M. ter Braack, A. Toncelli, M. Tonelli, O. Torre, E. Tournefier, F. Travasso, G. Vajente, J. F. J. van den Brand, C. Van Den Broeck, S. van der Putten, M. Vasuth, M. Vavoulidis, G. Vedovato, D. Verkindt, F. Vetrano, A. Viceré, J.-Y. Vinet, S. Vitale, H. Vocca, R. L. Ward, M. Was, M. Yvert, A. Zadrożny, and J.-P. Zendri. Advanced Virgo Status. In G. Auger, P. Binétruy, and E. Plagnol, editors, *9th LISA Symposium*, volume 467 of *Astronomical Society of the Pacific Conference Series*, page 151, January 2013.

[5] Kentaro Somiya. Detector configuration of KAGRA: The Japanese cryogenic gravitational-wave detector. *Class.Quant.Grav.*, 29:124007, 2012.

[6] V.B. Braginsky, M.L. Gorodetsky, and S.P. Vyatchanin. Thermo-refractive noise in gravitational wave antennae. *Physics Letters A*, 271(56):303 – 307, 2000.

[7] M. Cerdonio, L. Conti, A. Heidmann, and M. Pinard. Thermoelastic effects at low temperatures and quantum limits in displacement measurements. *Phys. Rev. D*, 63:082003, Mar 2001.

[8] V.B. Braginsky, M.L. Gorodetsky, and S.P. Vyatchanin. Thermodynamical fluctuations and photo-thermal shot noise in gravitational wave antennae. *Physics Letters A*, 264(1):1 – 10, 1999.

[9] M. De Rosa, L. Conti, M. Cerdonio, M. Pinard, and F. Marin. Experimental measurement of the dynamic photothermal effect in fabry-perot cavities for gravitational wave detectors. *Phys. Rev. Lett.*, 89:237402, Nov 2002.

[10] Stefan W. Ballmer. Photothermal transfer function of dielectric mirrors for precision measurements. *Phys. Rev. D*, 91:023010, Jan 2015.

[11] J.A. Sidles and D. Sigg. Optical torques in suspended fabryperot interferometers. *Phys. Lett. A*, 354(3):167 – 172, 2006.

[12] A. Perreca, J. Lough, D. Kelley, and S. W. Ballmer. Multidimensional optical trapping of a mirror. *Phys. Rev. D*, 89(12):122002, June 2014.

[13] Thomas Corbitt, Yanbei Chen, Edith Innerhofer, Helge Müller-Ebhardt, David Ottaway, Henning Rehbein, Daniel Sigg, Stanley Whitcomb, Christopher Wipf, and Nergis Mavalvala. An all-optical trap for a gram-scale mirror. *Phys. Rev. Lett.*, 98:150802, 2007.

[14] James Lough. *Optical Spring Stabilization*. PhD thesis, Syracuse University, 2014. Dissertations - ALL. Paper 172.

[15] D. Heinert, K. Craig, H. Grote, S. Hild, H. Lück, R. Nawrodt, A. Simakov, D. V. Vasilyev, D. P. Vyatchanin, S. and H. Wittel. Thermal noise of folding mirrors. *Phys. Rev. D*, 90:042001, Aug 2014.

[16] B. S. Sheard, M. B. Gray, C. M. Mow-Lowry, D. E. McClelland, and S. E. Whitcomb. Observation and characterization of an optical spring. *Phys. Rev. A*, 69(5):051801, 2004.

[17] E. D. Black. An introduction to Pound-Drever-Hall laser frequency stabilization. *Am. J. Phys.*, 69:79–87, 2001.

[18] S. W. Ballmer and D. J. Ottaway. New class of optical beams for large baseline interferometric gravitational wave detectors. *Phys. Rev. D*, 88(6):062004, 2013.

Curriculum Vitae

Title of Dissertation

Angular trapping of a mirror using radiation pressure

Full Name

David B. Kelley

Place and Date of Birth

Poughkeepsie, New York December 3, 1987

Colleges and Universities,	Years attended and degrees
Massachusetts Institute of Technology	2006–2010, B.S.
Syracuse University	2010–2015, Ph.D.

Publications

Awards and Fellowships

2010 Fellowship??

Major Department

Physics